Surfaces and Interfaces 56 (2025) 105640

Contents lists available at ScienceDirect

Surfaces and Interfaces

journal homepage: www.sciencedirect.com/journal/surfaces-and-interfaces

Unraveling the interaction of Ta atoms with Pt(111)☆

Kevin Bertrang [a], Tobias Hinke [a], Sebastian Kaiser [a], Matthias Knechtges [a], Federico Loi [b], Luca Sbuelz [b], Paolo Lacovig [c], Luca Bignardi [b], Friedrich Esch [a], Alessandro Baraldi [b,c], Sergio Tosoni [d], Aras Kartouzian [a,*], Ulrich Heiz [a]

[a] TUM School of Natural Sciences, Department of Chemistry, Chair of Physical Chemistry, Technical University of Munich, Catalysis Research Center, Garching D-85748, Germany
[b] Department of Physics, University of Trieste, 34127 Trieste, Italy
[c] Elettra-Sincrotrone Trieste, 34149 Trieste, Italy
[d] Dipartimento di Scienza dei Materiali, Università di Milano-Bicocca, 20125 Milano, Italy

ARTICLE INFO

Keywords:
Ta
Pt(111)
bi-metallic interface
HR-XPS
single atoms
sub-surface alloy
segregation

ABSTRACT

This study investigates the interaction between Ta and Pt by following the evolution of Ta atoms upon their evaporation in sub-monolayer quantities (~2 % ML) on a Pt(111) single crystal in vacuo at 40 K. Adsorption and bonding configurations are studied employing high-resolution X-ray photoelectron spectroscopy (HR-XPS). This is combined with density functional theory (DFT) calculations and reference measurements on atomically precise supported clusters that allow disentangling the contributions of distinct surface species to the complex Ta 4f spectra. The transient Ta atom mobility upon evaporation allows - besides atomic adsorption on the terraces - for atom migration to the Pt(111) step edges and the formation of small monolayer ad-islands even at 40 K. Interestingly, the Ta species bonded with Pt can be easily oxidized using a photon-induced O_2 dissociation process, showing the extremely high oxygen affinity of Ta even under the applied ultra-high vacuum (UHV) conditions. Annealing to 900 K leads to the sub-surface migration of Ta and the formation of a sub-surface alloy with Pt. Here, the extremely sharp Ta core-level components are observed at binding energies corresponding to a nominal oxidation state of +2, as confirmed by calculations of the projected density of states (pDOS). This sub-surface alloy is resistant to facile oxidation by atomic oxygen, unlike the Ta surface species that remain susceptible to oxidation. The oxide species and the sub-surface alloy are, however, perfectly interconvertible upon annealing to 900 K in vacuum, respectively in an oxygen environment, and thereby reveal an intriguing interplay between reductive intermixing of Ta and Pt and oxidative Ta segregation.

1. Introduction

The combination of two metals to form an alloy with beneficial electronic and chemical properties for instance for catalytic applications has been exploited since the 1960s [1,2]. Alloys demonstrate wide application potential, especially in catalytic hydrogenation or hydrocarbon reforming reactions [3–6]. In order to increase their performance in a tailored way, details on the true nanoscale morphology and bifunctionality are indispensable. The characterization of such materials down to atomic level is challenging considering the large variety of structures that can form. Alloying of a metal can occur in the bulk, sub-surface or surface region of a host metal. Alloys formed in the surface region largely differ from bulk alloys in terms of their chemical composition and structure and hence display distinguished chemical properties [3,7–9]. Reaction conditions and the chemical environment such as high temperatures or exposure to reactive gases as for example oxygen can induce alteration of the elemental composition and structure of an alloy. Diffusion of one of the alloy components may lead to segregation, which results in aforementioned changes and hence altered properties.

In this regard, the interaction between tantalum and platinum atoms, highly oxidizable the one and highly noble the other, is of great interest for several applications where new functionalities emerge, exploiting the interplay between surface intermixing and oxidation-induced

☆ Ta, Pt(111), bi-metallic interface, HR-XPS, single atoms, sub-surface alloy, segregation

* Correspondence author at. TUM School of Natural Sciences, Department of Chemistry, Chair of Physical Chemistry, Technical University of Munich, Garching D-85748, Germany; Catalysis Research Center, Garching D-85748, Germany.
E-mail address: aras.kartouzian@tum.de (A. Kartouzian).

https://doi.org/10.1016/j.surfin.2024.105640
Received 28 June 2024; Received in revised form 12 December 2024; Accepted 13 December 2024
Available online 16 December 2024

segregation. Examples that span a wide range of Ta oxidation states are, e.g., (i) the catalytic electro-oxidation of ethanol on TaPt nanoparticles, particularly prone to cleave C—C bonds [3], (ii) the controlled design of Pt interfaces with Ta sub-oxides in bi-metallic Ta-Pt memristor devices [10], and (iii) the metal-oxide-semiconductor contacts employing fully oxidized high-κ Ta dielectrics [11].

Several stoichiometric $TaPt_x$ (x = 1-3) bulk alloys have been synthesized and described in the literature [12,13]. However, surface alloys of Ta and Pt, especially those containing low densities of Ta (<15 %), and the interplay between oxidation/reduction and segregation/intermixing have scarcely been investigated. Surface segregation is the enrichment of one metal in the surface region of the other. The segregation behavior of Ta in Pt was simulated by Norskov et al. [14], who reported a highly unfavorable surface segregation energy (0.95 eV/atom). Alden et al. [15] found that the main contribution to the surface segregation energy derives from the surface free energy difference between both metals. This value has been experimentally determined as 0.66 eV/atom for Ta on Pt by Chandrasekaran et al. [16]. Thus, a strong anti-segregation, i.e. a favored intermixing, is predicted for Ta supported on Pt(111). Utilizing sub-monolayer coverages of metallic Ta and Ta oxides on a Pt(111) surface enables a bottom up approach to unravel fundamental insights about Ta and its oxides interacting with Pt [17–19]. In contrast to commonly employed sputter-etching techniques (top down), leading to interface corruption, our approach enables access to fundamental and unperturbed interfacial information [16].

Therefore, in this article, we study the arrangements that sub-monolayer quantities of supported Ta atoms adopt on Pt(111) directly after evaporation at low temperatures and upon annealing. We also investigate their tendency to react with atomic and molecular oxygen species. To this purpose, we employed synchrotron HR-XPS and exploit the high photon flux, tunable photon energy, and high energy resolution

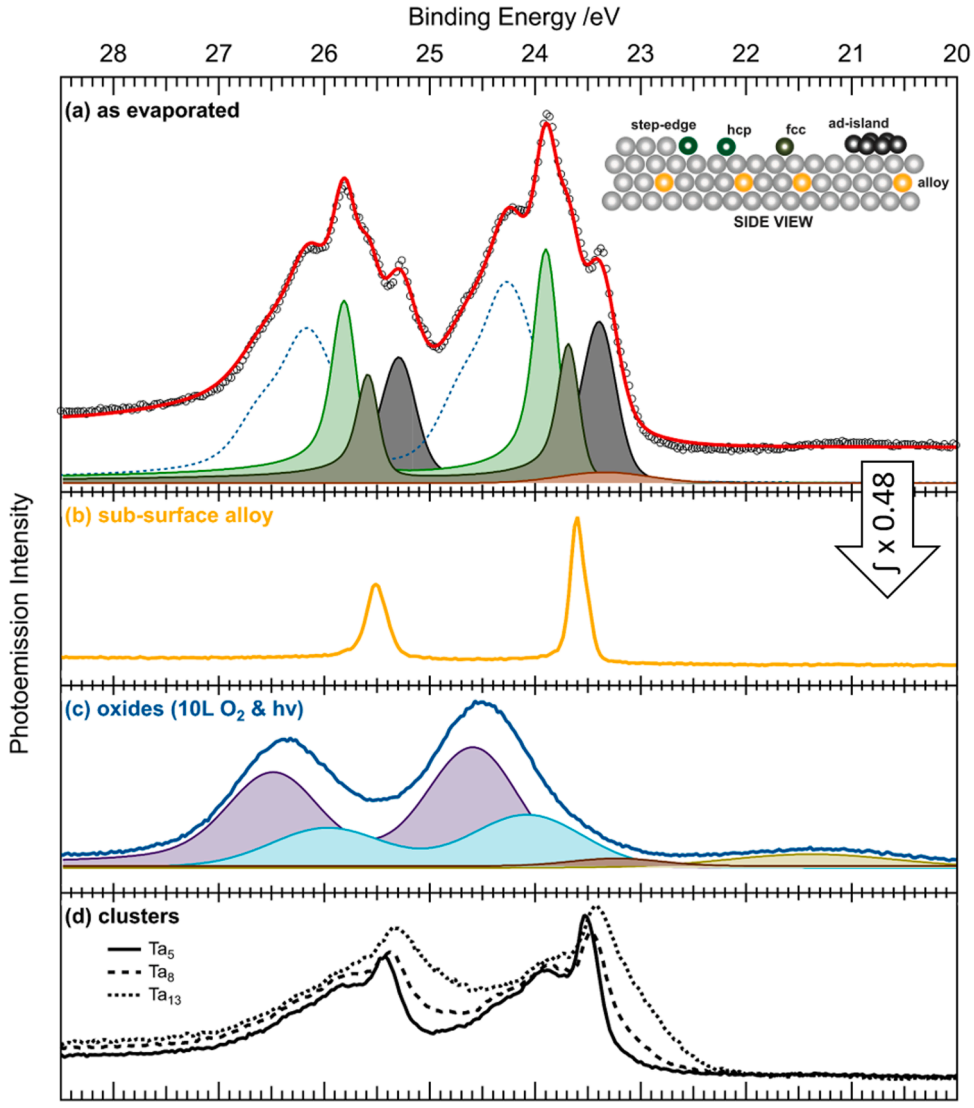

Fig. 1. Ta 4f XP spectra (hν = 150 eV) taken at 40 K. (a) Sub-monolayer Ta on Pt(111) (~2 % ML) evaporated at 40 K (figure 1(a) displays the same y-axis range of intensities as (b), (c) and (d), but with a rescaled axis by a factor of two for enhanced visualization of the fitting components). The experimental data (black circles) are decomposed into four fit components according to the on surface (Pt(111)) structures displayed in the upper right inset (Ta ad-islands in grey, Ta adatoms at fcc sites in dark green, Ta adatoms at step-edges and hcp sites in light green) and the residual Ta 4f signal, assigned to Ta oxides, in dashed blue with corresponding O 2 s emission in brown, (b) Ta-Pt sub-surface alloy (orange) formed after annealing to 900 K and entitled as alloy in the inset. The arrow indicates the ratio of the integrated areas of the emissions of (b) sub-surface alloy to (a) as evaporated. (c) Ta oxide 4f signal (turquoise and light purple) formed after exposure to 10 L O_2 at 40 K under X-ray irradiation (hν = 150 eV) together with O 2 s contributions (olive green and brown), and (d) size-selected Ta clusters with 5, 8 and 13 atoms deposited on Pt(111) at 40 K. Deposition of clusters yielded a coverage of 0.14 % ML 0.11 % ML and 0.06 % ML, respectively, in order to achieve a comparable amount of Ta atoms on the surface.

achievable at low temperatures (40 K, liquid helium cooling) to elucidate the Ta species present on Pt(111). The remarkable level of spectroscopic detail, with minimal spectral broadening by phonon excitation, enables capturing site-specific details of the interfacial interactions. We compare these results with previous experimental X-ray photoelectron spectroscopy (XPS) reports on Ta single crystals [20–22] and Ta-Pt nanoparticles [11,23,24], as well as Ta oxide thin-films [25,26], and support the assignment by DFT calculations that disentangle the contributions arising from different Ta arrangements. This combination unravels the morphological and electronic changes that Ta atoms undergo upon low-temperature deposition on Pt(111) upon further annealing and exposure to atomic and molecular oxygen. In particular, we observe an intriguing interplay between the reductive intermixing of Ta and Pt and oxidative Ta segregation.

2. Results and discussion

Sub-monolayer quantities of Ta atoms were evaporated on a Pt(111) single crystal. While thermally evaporated atoms typically have low kinetic energy, the high evaporation temperatures needed for Ta still lead to energies of 0.28 eV/atom (evaporation temperature of 2196 K, estimated via Clausius–Clapeyron for a low pressure [27]). The Ta atoms are thus soft-landed on the Pt(111) surface ($E_{kin} < 1$ eV/atom) [28], but with a residual energy sufficient to permit transient mobility [21–23]. According to the experimental quantification (Figure S1), a Ta coverage of ~2 % Ta atoms/Pt monolayer (with respect to the atom density of the Pt(111) surface which corresponds to 1.5×10^{15} atoms/cm^2) was obtained after a total evaporation time of 90 s. The freshly prepared sample was probed at a low temperature (40 K) by HR-XPS, as described in detail in the experimental section. The Ta 4f core level spectrum shown in Fig. 1(a) (black circles) has been acquired, as all Ta 4f core level spectra, at a photon energy of 150 eV, where the photoionization cross-section contrast with respect to the O 2 s energy level, occurring in the same binding energy (BE) spectral range, is maximized. At this photon energy, the overall energy resolution of about 50 meV allows us to distinguish a rich structure of spectral components arising from non-equivalent Ta atoms. All spectra shown in Fig. 1 were normalized with respect to the multiplicity of scans and the photon flux of the incident beam. For visualization of the fitting components, the axis of Fig. 1(a) was scaled by a factor of two. Note that the Ta 4f core level spectrum is characterized by a spin-orbit splitting of 1.91 eV and a branching ratio of 4:3 ($4f_{7/2}$:$4f_{5/2}$) [22]. The Ta 4f spectrum requires at least four different components to be decomposed, which are all considerably shifted towards higher BE with respect to metallic Ta^0 [21,22,29]. In order to experimentally disentangle the origin of the surprisingly large number of different core level components in Figure 1(a), we performed a series of experiments, in particular (i) annealing the low-temperature prepared sample to 900 K, without (Fig. 1(b)) and in the presence of a (molecular) oxygen atmosphere (Fig. 2(c)), (ii) letting the low-temperature prepared sample interact with beam-induced atomic oxygen prepared from physisorbed, molecular oxygen at low temperature (Fig. 1(c)) and (iii) separately depositing size-selected Ta clusters on clean Pt(111) at low temperature (Fig. 1(d)).

As shown in Fig. 1(b), after heating the sample to 900 K, the spectrum becomes very narrow, with a full width at half maximum (FWHM) of only 0.23 eV, which suggests the presence of a highly equivalent type of Ta species. According to previous DFT calculations intermixing is expected [14] and hence, we assign the narrow component at 23.59 eV to a TaPt alloy. In order to confirm this assignment, we tested the Ta local environment by trying to oxidize the sample using two different strategies: on the one hand (Fig. 2(**i**)) by exposing to X-ray beam-induced atomic oxygen formation at 40 K (method described in Ref. [30]) and on the other hand (Fig. 2(**ii**)) by exposing the surface to O_2 ($p = 1 \times 10^{-6}$ mbar) during a heating ramp of up to 900 K. Despite the

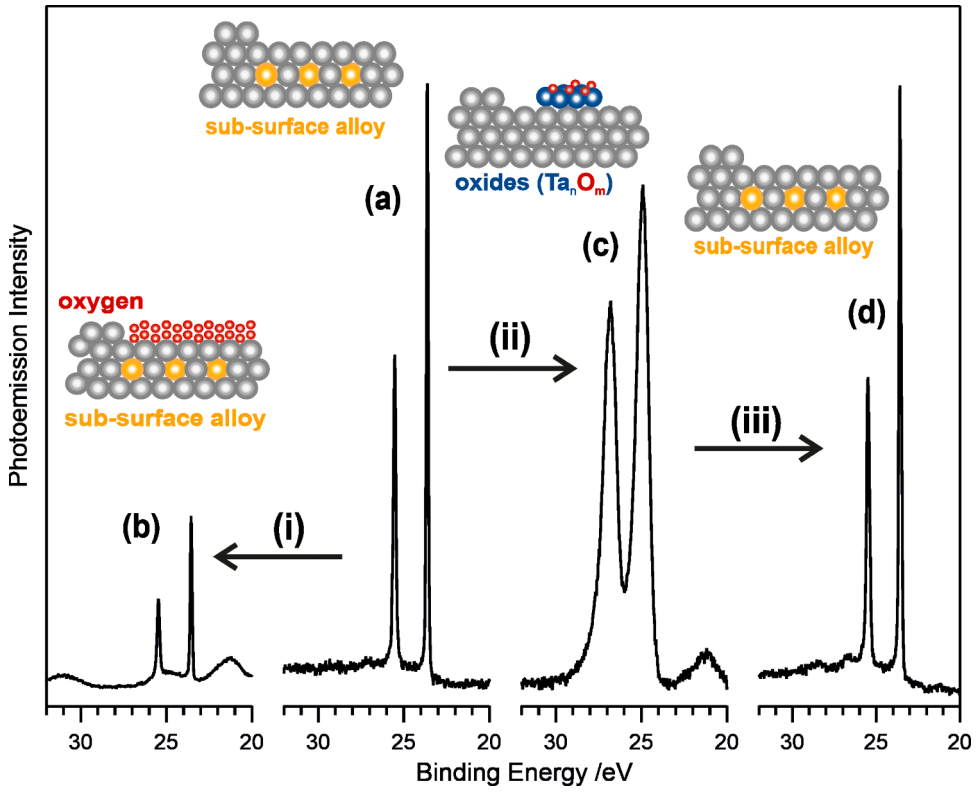

Fig. 2. Ta 4f XP spectra ($h\nu = 150$ eV) recorded at 40 K, indicating the reactivity of the sub-surface alloy (a), formed as shown in Figure 1(b). While (i) physisorption of O_2 (10 L) at 40 K induces only a signal attenuation but no oxidation via X-ray induced atomic oxygen (b), (ii) high-temperature exposure to molecular oxygen (1×10^{-6} mbar at 900 K) leads to the formation of oxidic species (c) that can (iii) again be interconverted into the sub-surface alloy by reductive annealing in vacuum at 900 K (d).

high oxygen affinity of Ta, no reaction is observed upon atomic oxygen production at low temperature, a strong indication for sub-surface migration of the Ta atoms into the Pt support upon annealing to 900 K (Fig. 2(a)). Note that the physisorbed O_2 overlayers on Pt(111) lead to an attenuated Ta 4f emission (Fig. 2(b)) and display emissions identified at 31 eV [31]. In contrast, the oxidation with $p(O_2) = 1 \times 10^{-6}$ mbar at 900 K succeeded and yielded oxidic Ta $4f_{7/2}$ spectral components ranging between 24 - 25 eV, as shown in Fig. 2(c). This spectrum is similar to the spectrum yielded from oxidation of as evaporated Ta (Fig. 1a) with beam-induced atomic oxygen at 40 K, see Fig. 1(c). While one would expect that Ta assumes its highest, +5 oxidation state (BE(Ta $4f_{7/2}$) > 26 eV) [18,26], the observed lower BEs indicate a lower formal oxidation state [32]. The oxidic peaks are observed in the same energy range as the residual intensity in the pristine spectrum of Fig. 1(a), corroborating the assignment to oxidic species. Concomitantly, an oxygen related 2 s emission at ~ 21 eV indicates the presence of atomic oxygen at Pt(111) formed upon X-ray irradiation of adsorbed oxygen at 40 K, visible in Fig. 2(b) and (c).

Interestingly, subsequent annealing of the oxides to 900 K in UHV results in a complete reduction of the oxide and again in the formation of the sub-surface alloy with the same characteristic Ta 4f core level spectrum (see Fig. 2(d)). The reversible interconversion of the oxidic species into the alloy could be repeated over at least two cycles without loss of Ta. The integral in figure S2 is reduced by the same amount (0.48) as shown in Fig. 1(a-b). Once the alloy has formed, no significant decrease in the overall Ta 4f intensity was observed neither over longer annealing times nor upon cyclic interconversion between the alloy and the oxides, thus excluding the process of Ta migration into the bulk of Pt. Under oxygen-free, reductive conditions, we observe the reversible sub-surface penetration of Ta into the Pt support, which indicates intermixing, while the presence of oxygen leads to the surface segregation upon Ta oxide formation. The large Ta-O bond formation energy might promote this process. Comparing the integrated area of the spectrum after alloy formation (Figure 1(b)) with the integrated area directly after Ta deposition (Fig. 1(a)) yields a ratio of 0.48. This is in good agreement with the expected intensity attenuation (0.51) due to the increased distance traveled by an electron through a Pt layer for Ta situated in the second layer of the Pt support, as described in literature [33]. In order to elucidate on the arrangement of Ta in the Pt surface layers subsequent to annealing, spectra of Ta 4f orbital emissions with various beam energies (150 eV, 400 eV, 650 eV) were measured, to probe Ta depth distribution for the as deposited, oxidized and alloyed samples. The data were inconclusive for all samples (oxide, alloy, as deposited). The integrals as a function of beam energy display strong variations with no apparent trend or consistency. The origin of this unexpected trend can be explained in terms of photoelectron diffraction effects that are commonly known to induce unexpected modulation in the photoemission intensities especially in the case of ordered surface, such as in our Pt (1111) single crystal [*34*,*35*].

In the following, we discuss these findings and assignments in the light of DFT calculations for Ta adatoms on the Pt support and atoms embedded into the Pt support. Table 1 summarizes the observed adsorption energies (E_{ads}) and compares the experimentally observed core electron BEs to the calculated ones. The latter are aligned to the experimental BEs by applying an internal experimental reference (IER) (see Experimental Section): for the Ta 4f spectra, we used the experimental BE of the very sharp sub-surface alloy peak found at 23.59 eV as IER_{Ta} and shifted the calculated value for second-layer substitutional Ta atoms to that value and all other calculated BEs accordingly.

According to the DFT results, sub-surface configurations are remarkably preferred with respect to fcc or hcp adsites (by > 1 eV). Thermodynamically, the incorporation of Ta into the Pt surface layers is thus favored compared to the adsorption on the Pt surface, in line with the tendency towards intermixing of Ta atoms in a Pt matrix reported previously in both, theoretical [14] and experimental works [16]. Even though the calculations indicate the highest E_{ads} for Ta atoms at step edges (−10.29 eV), solely sub-surface species are observed after annealing to 900 K, presumably due to entropic effects.

Table 1
Computed adsorption energies (E_{ads}), calculated Ta $4f_{7/2}$ BE (after IER realignment), and experimental BE (obtained from fits) of Ta in different ad- and substitutional sites. In order to limit the fitting parameters experimental BEs of non-equivalent Ta adatom species in hcp, bridge sites and at step-edges are grouped as a single component.

BEs of Ta $4f_{7/2}$ Ta configuration	E_{ads} (eV)	Calc. BE (eV)	Exp. BE (eV)
Ta adatoms			
hcp	−3.84	23.77	
Bridge	−3.68	23.82	23.88
Step-edge	−10.29	23.79	
fcc	−3.84	23.62	23.67
Ad-islands	−3.25	23.42	23.38
Substitutional Ta			
First layer (L1)	−5.16	23.59	–
Second layer (L2) (sub-surface alloy)	−6.58	23.59	23.59
Third layer (L3)	−6.42	23.45	–
Ta references		23.59	
IER_{Ta}		23.59	23.59
Ta(110) rel. to IER_{Ta}		22.12	–

Although other phenomena than the formation of a Ta-Pt sub-surface alloy, such as the Ta incorporation in the Pt surface due to the strong interaction between Ta and Pt might also lead to a similar observation (non-oxidizable with atomic oxygen, highly ordered Ta species yielding very narrow Ta 4f orbital emissions and no considerable loss of signal integral upon repetitive annealing to 900 K), based on the support delivered from the theoretical calculations and in the absence of other complementary experimental evidence we consider this option to be more likely.

The process of Ta diffusion into the Pt sub-surface layers can be observed upon annealing in UHV to temperatures above 900 K, while it is expected to be kinetically hindered at the low temperature of 40 K. However, the calculated surface diffusion barrier for Ta adatoms diffusing between hcp sites along a hcp-bridge-hcp path is small (0.16 eV), thus indicating that the kinetic energy of 0.28 eV/atom of the soft-landing Ta atoms could easily promote their transient surface diffusion as adatoms [36]. Besides migration to steps, the aggregation to form small ad-islands can also be envisaged, leading to a new Ta 4f spectral component. To experimentally attribute the observed peak at 23.38 eV in Figure 1(a) (grey) to small Ta ad-islands, we deposited in a separate experiment atomically precise Ta_n clusters of size $n = 5, 8, 13$ by a laser ablation cluster deposition setup that ensures precise coverage control and soft-landing conditions [37]. The comparison of their XP spectra in Figure 1(d) shows a pronounced photoemission peak at about 23.4 eV, which shifts, with increasing size towards lower BEs. In general, increasing the size of metallic particles leads to a BE shift towards Ta bulk associated emissions. A systematic analysis of this size dependence will be the topic of a future article. From a rough, direct comparison, the ad-island peak maximum in Fig. 1(a) matches most that of Ta_{13}.

Considering the morphology of these clusters, in light of the modelling by DFT, the general trend for metal-supported metal clusters, such as Ag_{19} on Pt(111) [38] or Pd_{19} on Rh(111) [39], and the strong interaction between Ta and Pt, points to the formation of single-layer high Ta ad-islands [40]. This two-dimensional cluster geometry is indeed confirmed by the scanning tunneling microscopy (STM) image in Fig. 3, which shows Ta_8 clusters deposited and measured on Pt(111) at room temperature. The clusters appear as bright protrusions on the surface, are randomly distributed, and maintain their monodispersity upon deposition. No preferential cluster adsorption at step edges is observed, indicating that the clusters are immobile at T = 300 K, at least within the timeframe of the entire measurement (several hours). The height histogram taken over the entire terrace reveals a single apparent height of 0.15 nm. which is smaller than the atomic step height of a Pt

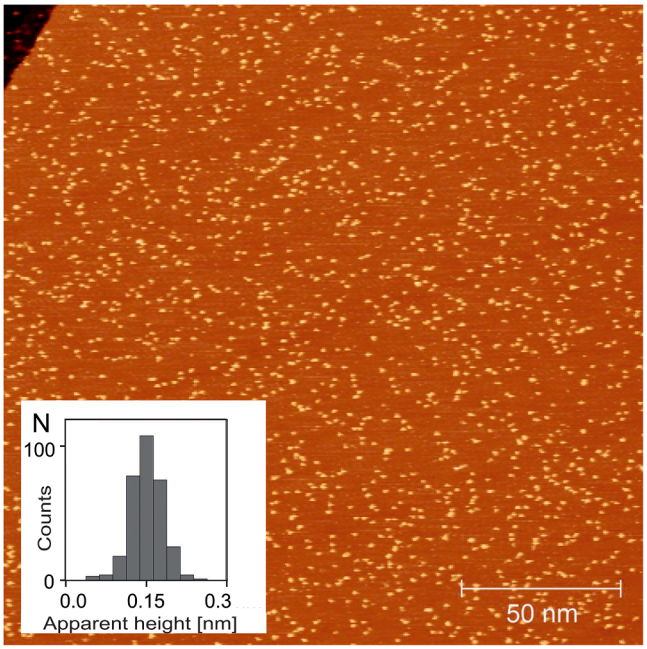

Fig. 3. STM image of Ta_8 clusters deposited and measured on Pt(111) at room temperature (0.04 clusters/nm^2). The height histogram (inset) clearly indicates that exclusively single-layer high clusters are formed, indicating monodisperse deposition. The clusters do not preferentially decorate the step in the upper left, pointing to their immobility at this temperature. Imaging parameters: 1.5 V, 0.3 nA.

(111) surface (0.226 nm) [41]. This value can be rationalized by the different densities of states of the two involved metals that strongly influence the observed heights in the STM topography of heteroepitactic contacts.

Since we deposit atoms of limited mobility with our evaporator, the remaining and strongly pronounced metallic Ta 4f contributions at 23.5–24.0 eV are tentatively interpreted as single Ta adatoms dispersed on the Pt(111) support. Here, the assignment to adatoms on hcp or fcc sites or at step-edges requires the support of the DFT calculations.

While the computational results exclude the presence of Ta atoms in top sites – that spontaneously relax towards nearby hollow sites – Ta adatoms in hcp and fcc three-fold sites on flat Pt(111) terraces are equally probable due to similar adsorption energies. However, the most favorable adsorption site for Ta adatoms is found at step-edges (E_{ads} = -10.29 eV). The peak observed at 23.88 eV is in good agreement with the calculated BE of 23.79 eV for step-edge adsorption. This site can be reached by the evaporated Ta atoms due to their transient mobility. Due to its particular stability, it could also act as a nucleation center for the Ta ad-island formation. However, Ta adatoms in hcp and bridge sites have similar BEs and thus cannot be distinguished in the single fit contribution at 23.88 eV (light green peak in Fig. 1(a)). Fcc sites, on the other hand, can be distinguished by their different BE. The calculated value of 23.62 eV fits well with the clear shoulder at 23.67 eV (dark green peak in Figure 1(a)) that we assign hence to Ta adatoms in fcc sites. Similar adsorption energies for Ta adatoms in fcc and hcp sites may suggest the same adatom contribution at the two sites, see Table 1. Thus, one can argue, that the area of the light green peak includes an intensity due to hcp sites which is expected to be close to the one of the dark green peak (fcc). The remaining intensity of the light green peak is attributed to step-edges and bridge sites.

In the Pt 4f spectra ($h\upsilon$ = 220 eV) reported in Figure S2(c,d), only minor variations with respect to the clean Pt(111) surface are expected due to the evaporation of low Ta coverages. We, therefore, present the difference spectra as well, which reveal, first, a reduced intensity of the Pt(111) surface component at 70.52 eV, as expected for Ta adatoms that form a new bond with the Pt surface, in line with similar examples such as Pt adatoms on Pt(111) [42], Rh adatoms on Rh(111) and Rh(100) [43] or Pt adatoms on Rh(111) [44]. The loss of the surface component in the case of Ta adatoms on Pt(111) as depicted in figure S2(d) is less pronounced than for the formed alloy S2(c) and the expected new component presumably measurable in the range of bulk Pt emissions. While the decrease of the clean surface component is a sign of site occupation and can be used quantitatively for the evaluation of the amount of the ad-species (only for very low coverages) the expected growth of new components can be affected by scattering and photoelectron diffraction effects, which could result in a strong dampening of the signal. Photoelectron diffraction effects have readily been observed and can account for intensity modulations up to 40 % and higher [*34*, *35*].

In addition, the difference spectrum upon annealing to 900 K - when the sub-surface alloy is formed - (Figure S2(c)) clearly shows a new component appearing at around 71.20 eV. The integral of the new signal in the difference spectrum is comparable to the loss of surface component integral. This peak can be assigned to Pt atoms in alloy configurations with Ta atoms, as a comparison with literature values for $TaPt_x$ (x = 1-3) nanoparticles (71.50 eV) [45], and for other bi-metallic Pt compounds such as Pt-Fe (71.40 eV) [46] reveals. The alloy formation is further backed by our calculations of Pt 4f with a BE value of 71.01 eV (See Figure S2). Ta 4f BEs of substitutional Ta atoms embedded into Pt surface and sub-surface layers were simulated (see Table 1), with values of 23.59 eV (IER_{Ta}) calculated for Ta atoms sitting in the first or second layers, and values of 23.45 eV for Ta atoms sitting in the third Pt(111) layer. This is, again, in good agreement with the values found for $TaPt_x$ (x = 1-3) nanoparticles (23.57–23.61 eV) [45], and within the broad range of BEs observed for Ta-Pt bulk materials (22.6 eV-23.6 eV) [11]. The BEs do not allow the assignment of the surface layer, in which the Ta atoms reside, which could tentatively be assigned to the second surface layer by considering the observed attenuation (see above). However, a low coverage of Ta atoms and the overlap with O 2 s related emissions prevents a rigorous and accurate quantitative study with respect to Ta fractions and their individual change in oxidation state. The alternative to measure the 4d level of Ta instead of the Ta 4f introduces two significant limitations related to (i) the reduced cross-section compared to the 4f level (at the photon energies available at the SuperESCA, it is 1 to 2 orders of magnitude lower) and (ii) a much larger intrinsic width than that of the 4f levels, which thus prevents resolving spectral components caused by non-equivalent atomic configurations. Overall, the Ta 4f BEs, observed on Pt(111) for Ta ad- and embedded atoms, as in Figure 1(a, b), are shifted considerably to higher BEs compared to the value found in the literature for pure Ta bulk and surface species, *e.g.* Ta bulk (21.64 eV) [21,22,29]; Ta(100) surface (22.39 eV) [29]; Ta(110) surface (21.97 eV) [22]; Ta(111) surface (22.04 eV) [21]. In the frame of the tight-binding model, the considerably higher work function [47] of Pt leads to a depletion of the valence band of Ta when interacting with Pt, and hence to a narrowing of its less than half-filled D-band and a core level shift (CLS) to higher BE [48]. Similar BE shifts (Δ_{BE} = 1.5-1.9 eV) have been observed by Kerrec et al. when preparing Ta oxide species in a low oxidation state, namely Ta^{1+} and Ta^{2+} [49]. Indeed, a simple Bader charge analysis of the calculated pDOS, reported in Figure S3, points to an apparent oxidation state close to +2 for all Ta species. Altogether, this points to an immediate oxidation of Ta atoms in contact with the Pt(111) surface – already as adatoms at 40 K, and as well as sub-surface alloy upon annealing to 900 K in UHV. Interestingly, these Ta adatoms show a 200-300 meV higher BE than the substitutional Ta atoms that are coordinated to even more Pt atoms. Here, the overall atomic coordination number, changing from 3 to 12, seems to be decisive, analogously to exposed Ta crystal surfaces [29], where the undercoordination leads to a redistribution of valence electrons resulting in a shift towards higher Ta 4f BEs.

At this stage, we remain with the interpretation of the residual components appearing at BEs larger than 24 eV, shown in blue in Fig. 1

(a). The large FWHM of the main peak at 24.3 eV and at least one pronounced shoulder at 24.8 eV indicate a superposition of several oxides that cannot be disentangled in a simple approach, which is further hampered by a possible overlap with O 2 s emissions from H_2O and chemisorbed oxygen [50,51]. However, the spectra resemble those of the oxidic species obtained after high-temperature oxidation by 10 L O_2 (Fig. 1(c)), tentatively fitted by two components. The XPS literature on Ta oxides assigns Ta 4f peaks in the region 22.5-24.0 eV to Ta species with oxidation states between +1 to +4 [32,49,52]. In contrast, the oxidation state +5 is commonly observed at BEs larger than 26 eV [32, 49]. Interestingly, we do not observe the appearance of fully oxidized Ta^{5+} that would be expected upon oxidation of this highly oxophilic metal. The O 1 s spectrum (shown in Figure S4, with a significantly lower signal-to-noise ratio) confirms the presence of oxides on the Pt (111) surface and suggests the presence of Ta in oxidation states +3 (529.4 eV [53]) and +5 (531.5 eV [49,54]), but has overlapping signals originating from adsorbed H_2O and CO (>532 eV – further confirmed by the C 1 s spectrum in Figure S5) that prevent a clear oxidation state assignment based on the O 1 s signals. Both molecular species are also prominent adsorbates on Pt(111) at low temperatures under UHV conditions. Moreover, H_2O can efficiently break-up by soft X-ray irradiation, yielding hydroxyls and atomic oxygen that readily reacts with the Ta atoms present on the surface. This explains, together with the oxophilicity of Ta, that even minor oxygen traces in the background during the evaporation process, lead to the presence of Ta oxides from the beginning on, even on the freshly deposited sample in Fig. 1(a).

3. Conclusion

In the present work, we have investigated the interaction of sub-monolayer Ta atoms with Pt(111) to elucidate their intermixing and segregation behavior. After evaporation onto the pristine surface at 40 K, the system was annealed and oxidized in beam-induced atomic and in molecular oxygen, respectively, and studied by HR-XPS measurements in combination with DFT calculations to disentangle the complex Ta 4f spectra.

Upon evaporation, the Ta atoms present transient mobility so that a fraction either reaches step edges or forms small monolayer ad-islands, even at low temperatures. This ad-island assignment is confirmed by the deposition of size-selected cluster samples for reference spectra and STM imaging. Under the conditions used in our experiments, we showed that when a low coverage (~2 % ML) of Ta atoms is in contact with the Pt support, whether as single adatoms, at steps or in ad-islands, Ta gets immediately oxidized. The strong interaction between metallic Ta particles (both atoms and clusters) and Pt, which is evidenced by the considerably shifted BEs compared to BEs of Ta bulk materials and Ta surfaces, leads to a redistribution of the electron configuration expressing similar CLSs to lower Ta oxides. This in combination with the computationally yielded charge from Bader charge analysis, suggests the oxidation of Ta atoms and clusters when in contact with the Pt surface.

Furthermore, its oxophilicity leads to the formation of oxides even under the applied UHV conditions. The Ta oxides observed at the Pt (111) surface either upon deposition, by reaction with oxygen bearing molecules (H_2O, CO) or after oxidation by either molecular oxygen at 900 K or by atomic oxygen at 40 K, express even larger CLSs compared to metallic Ta. The duality between Pt and oxygen induced oxidation of Ta is complex, as CLSs are observed after oxidation with oxygen, which are not identified in literature. A straightforward interpretation is not accessible without further consideration of e.g. structural aspects as Ta oxide morphology and binding configuration to the Pt(111) surface. The latter in particular is beyond the scope of this manuscript and thus the subject of our upcoming study.

Annealing the sub-monolayer Ta layer on Pt(111) to 900 K in vacuum – and thus reducing the oxides – leads to the formation of a sub-surface alloy with extremely sharp Ta 4f core level peaks at a binding energy that corresponds to a nominal oxidation state of +2. While this sub-surface alloy resists oxidation in beam-induced atomic oxygen, since not spatially directly accessible, it can be reoxidized with molecular oxygen at elevated temperatures (900 K). This interconversion between buried alloy species (intermixing) and a Ta surface oxide (segregation) can be precisely followed in the HR-XPS spectra and is fully reversible, without Ta loss into the bulk of Pt. Our study thus unravels the conditions for perfect layer control on Ta-Pt interfaces and paves the way for redox recovery strategies of less-defined structures.

4. Experimental section

Sample preparation. All experiments were performed in a UHV chamber at a base pressure of 10^{-10} mbar. A Pt(111) single-crystal (0.78 cm^2, 4 N, Mateck) was prepared by subsequent cycles of sputtering with Ar^+-ions (E_{kin} = 1.5 keV, $p_{Ar} = 3.6 \times 10^{-6}$ mbar, I = 10 μA, 300 K, 20 min) followed by flash annealing to 700 K. Heating is enabled by an electron beam from a resistively heated W-filament on the back of the sample. Remaining carbon impurities were removed by annealing in an O_2 atmosphere ($p = 1 \times 10^{-7}$ mbar, 870 K, 5 min), followed by the removal of adsorbed oxygen in H_2 atmosphere ($p = 5 \times 10^{-8}$ mbar, 670 K, 5 min). The process was repeated until no more contaminations were identified in the O 1 s, C 1 s, Ta 4f and Pt 4f regions.

Ta evaporation was performed on the Pt(111) crystal at 40 K. Prior to evaporation, the substrate was flash annealed up to 500 K in order to remove adsorbates accumulated from the chamber background. The atoms were then evaporated from a Ta wire (thickness: 0.125 mm, purity: 99.9 %, Goodfellow) using an in-house built wire evaporator with resistive heating. For cleaning, the evaporator housing and the Ta wire were degassed and subsequently exposed to H_2 (10^{-7} mbar, 600 K, 10 min) for several cycles. Evaporation was performed at a power of 14 W in time windows of limited duration (< 30 s) to reduce heating of the crystal and hence minimize atom mobility and, thus, particle agglomeration. The evaporated atoms have a low kinetic energy (~0.28 eV/atom) [55,56].

Oxidation. The oxidation of evaporated Ta atoms and sub-surface alloy at 40 K was performed according to previously reported procedures [21,42]. Oxygen was pre-dosed at 40 K (10 L), yielding a physisorbed layer of molecular O_2. Irradiation of the sample with soft X-rays leads to the emission of secondary electrons that split the physisorbed O_2 to form highly reactive atomic oxygen, which permits to reach the highest accessible oxidation state of adsorbed particles [30]. Oxidation of the sub-surface alloy by molecular oxygen, instead, was performed at 900 K, by exposing the system to 1 × 10–6 mbar of O_2 for five minutes. As exemplarily shown in Figure S6, such an oxidation treatment, applied to Ta_8 clusters, leads to the formation of larger oxide islands that are predominantly flat and have diameters of a few nanometers. Oxidized Ta is subsequently transformed back into the sub-surface alloy by annealing the sample in UHV at 900 K for five minutes.

High-resolution XPS. The SuperESCA beamline of the ELETTRA synchrotron radiation facility (Trieste, *Italy*) was used for *in-situ* HR-XPS with an electron energy of 2.0 GeV. In the photon energy range applied here for the Ta 4f and Pt 4f spectra, a resolution better than 50 meV can be achieved, with a decreasing resolution for higher beam energies [57]. Photoelectrons were collected and filtered using a Phoibos 150 mm mean-radius hemispherical electron energy analyzer (SPECS, *Germany*) in fixed analyzer transmission mode and detected with a delay line detector. A typical measurement set for probing different orbitals, with the corresponding photon energies indicated in brackets, consisted of the following: O 1 s ($h\nu = 650$ eV), C 1 s ($h\nu = 400$ eV), Pt 4f ($h\nu = 220$ eV) and Ta 4f ($h\nu = 150$ eV). All spectra were measured in normal emission geometry, with magic angle orientation between incident beam and analyzer. The analyzer was operated in fixed analyzer transmission at a pass energy of 5 eV except for the Ta 4f spectra measured at 400 eV and 650 eV where a pass energy of 10 eV was used. For reference of the core electron binding energies all spectra were aligned with respect to the Fermi energy measured under the same conditions. Furthermore, all

spectra were normalized to the photon flux of the incident beam and the number of scans. The Ta 4f spectra recorded at various beam energies (150 eV, 400 eV, 650 eV) were additionally normalized to the respective cross-section, to the analyzer transmission function and the secondary electron background. A linear background was included in the fitting procedure and subtracted before integration of the Ta 4f signal. In order to align the computed core-electron binding energies to the experimental values, we first calculated the defect-free Ta(110) slab (19.35 eV) and the Ta 4f CLS of the surface alloy formed at 900 K (+1.47 eV) with respect to the slab. The sub-surface alloy is experimentally found at 23.59 eV and used here as an IER_{Ta} measured under the same conditions as all non-equivalent Ta species. The realigned Ta(110) emission (22.12 eV) with respect to the IER_{Ta} is in good agreement with experimental values [22]. Using the same approach, the calculated Pt 4f BEs of surface atoms in Pt(111) were calibrated with respect to the experimental value of 70.52 eV corresponding to the surface peak in Pt(111) [58]. The emission from non-radial symmetric orbitals (Pt 4f, Ta 4f) was fitted with Doniach-Šunjić functions [59,60], which are commonly used to fit 4f core levels of 5d transition metals [61,62] using a linear background. A Lorentzian width (Γ) of 0.08 eV was extracted from the sharp emission of the sub-surface alloy. This value was adopted for the fit of all Ta 4f emissions. The asymmetry factor yielded $\alpha = 0.10\text{-}0.14$. A Gaussian function was used to fit the O 2 s contributions.

Computational details. All calculations are performed with the code VASP6 [63,64]. The interaction between the core electrons and the nuclei is described with the PAW formalism [65,66]. The plane-waves basis set is expanded up to a kinetic energy of 400 eV. Truncation criteria of 10^{-5} eV for the electronic loop and 0.01 eV/Å for the ionic loop are set. The PBE exchange-correlation functional is adopted [67]. The reciprocal space is sampled with a Monkhorst net of $4 \times 4 \times 1$ K-points. Pt(111) is modeled with a five-layer slab, where the atoms from the bottom layer are frozen in their bulk positions while all other atoms are free to relax. An empty space of at least 20 Å is included in all supercells to avoid spurious interactions with the replica. The core level energies are calculated within the initial state approximation. Final state effects surely play an important role for the interpretation of CLSs in alloys [68–70], as the screening effect of the support, e.g. Pt(111) acts as a perturbation on the Ta 4f core hole. Calculations only concerning initial state shifts are often found to yield a reasonable agreement with experimental findings for both metal adlayers and bulk alloys [71]. Thus, suggesting that shifts from initial state effects, *e.g.* a change in oxidation state, which are commonly expressed by differences up to several eV, can be understood without invoking final state effects. Accordingly, we rely on the frozen-core approximation, which neglects the final state effects and relies on the energy of the eigenvalues corresponding to semi-core states as a measure of the BE.

CRediT authorship contribution statement

Kevin Bertrang: Writing – review & editing, Writing – original draft, Investigation, Formal analysis, Data curation. **Tobias Hinke:** Writing – review & editing, Writing – original draft, Investigation, Formal analysis, Data curation. **Sebastian Kaiser:** Writing – review & editing, Writing – original draft, Validation, Investigation. **Matthias Knechtges:** Investigation. **Federico Loi:** Writing – review & editing, Methodology, Investigation. **Luca Sbuelz:** Investigation. **Paolo Lacovig:** Resources, Methodology, Investigation. **Luca Bignardi:** Investigation. **Friedrich Esch:** Writing – review & editing. **Alessandro Baraldi:** Writing – review & editing, Supervision, Methodology. **Sergio Tosoni:** Writing – review & editing, Writing – original draft, Formal analysis, Data curation. **Aras Kartouzian:** Writing – review & editing, Writing – original draft, Supervision, Project administration, Investigation, Formal analysis, Conceptualization. **Ulrich Heiz:** Writing – review & editing, Funding acquisition.

Declaration of competing interest

There is no conflicts of interest.

Funding Sources

The Fond Nationale de la Recherche Luxembourg for financial support (Kevin Bertrang, grant ID 14559324). The research at TUM has been financed through the DFG (Project HE3454/23–2).

Acknowledgments

T.H. and K.B. would like to thank R. Lazzari (CNRS, Paris) for developing the I4P (Igor Pro Paris Photoemission Package) and making it available for free. A.B. gratefully acknowledges the financial support from the MUR-PRIN 2022 project n. 20222FXZ33 entitled “ Materials modelling for energy storage applications”. S.T. acknowledges financial support from ICSC – Centro Nazionale di Ricerca in High Performance Computing, Big Data and Quantum Computing, funded by European Union – NextGenerationEU and computational support from CINECA supercomputing centre.

Abbreviations

HR-XPS, high resolution X-ray Photoelectron Spectroscopy; DFT density functional theory; UHV, ultra-high vacuum; pDOS, projected density of states; XPS, X-ray photoelectron spectroscopy; CLS, core level shift; BE, binding energy; STM, scanning tunneling microscopy; IER, internal experimental reference

Supplementary materials

Supplementary material associated with this article can be found, in the online version, at doi:10.1016/j.surfin.2024.105640.

Data availability

Data will be made available on request.

References

[1] H. Swift, Metallic phases and activities of nickel-tin-silica catalysts Dehydrogenation of cyclohexanone, cyclohexanol, and cyclohexane, J. Catal 12 (1) (1968) 5–14, https://doi.org/10.1016/0021-9517(68)90067-5.
[2] H.C. Eckstrom, Catalysis by metals (Bond, G. C.), J. Chem. Educ. 40 (2) (1963) A146, https://doi.org/10.1021/ed040pA146.
[3] R.T. Hannagan, G. Giannakakis, M. Flytzani-Stephanopoulos, E.C.H. Sykes, Single-atom alloy catalysis, Chem. Rev. 120 (21) (2020) 12044–12088, https://doi.org/10.1021/acs.chemrev.0c00078. Published Online Jun. 26, 2020.
[4] J.H. Sinfelt, Catalysis by alloys and bimetallic clusters, Acc. Chem. Res. 10 (1) (1977) 15–20, https://doi.org/10.1021/ar50109a003.
[5] G. Bai, X. Wen, L. Niu, Recent developments in amorphous alloy catalysts for hydrogenation. Reference Module in Chemistry, Molecular Sciences and Chemical Engineering, Elsevier, 2016, https://doi.org/10.1016/B978-0-12-409547-2.11034-0.
[6] M.R. Ball, K.R. Rivera-Dones, E.B. Gilcher, S.F. Ausman, C.W. Hullfish, E.A. Lebrón, J.A. Dumesic, AgPd and CuPd catalysts for selective hydrogenation of acetylene, ACS Catal 10 (15) (2020) 8567–8581, https://doi.org/10.1021/acscatal.0c01536.
[7] W.D. Song, J.F. Ying, W. He, V.Y.-Q. Zhuo, R. Ji, H.Q. Xie, S.K. Ng, S.L.G. Ng, Y Jiang, Nano suboxide layer generated in Ta2O5 by Ar+ ion irradiation, Appl Phys Lett 106 (3) (2015) 1951, https://doi.org/10.1063/1.4906395.
[8] M.T. Darby, F.R. Lucci, M.D. Marcinkowski, A.J. Therrien, A. Michaelides, M. Stamatakis, E.C.H. Sykes, Carbon monoxide mediated hydrogen release from PtCu single-atom alloys: the punctured molecular cork effect, J. Phys. Chem. C 123 (16) (2019) 10419–10428, https://doi.org/10.1021/acs.jpcc.9b01213.
[9] H.L. Tierney, A.E. Baber, J.R. Kitchin, E.C.H. Sykes, Hydrogen dissociation and spillover on individual isolated palladium atoms, Phys. Rev. Lett. 103 (24) (2009) 246102, https://doi.org/10.1103/PhysRevLett.103.246102. Published Online Dec. 10, 2009.
[10] K. Skaja, M. Andrä, V. Rana, R. Waser, R. Dittmann, C. Baeumer, Reduction of the forming voltage through tailored oxygen non-stoichiometry in tantalum oxide ReRAM devices, Sci. Rep. 8 (1) (2018) 10861, https://doi.org/10.1038/s41598-018-28992-9. Published Online: Jul. 18, 2018.

[11] C.-F. Huang, B.-Y. Tsui, Ta–Pt alloys as gate materials for metal–oxide–semiconductor field effect transistor application, Jpn. J. Appl. Phys 48 (3) (2009) 31202, https://doi.org/10.1143/JJAP.48.031202.

[12] B.C. Giessen, R.H. Kane, N.J. Grant, On the constitution diagram Ta-Pt between 50 and 100 At. PCt Pt, Trans. Met. Soc. AIME (233) (1965).

[13] E. Bucher, F. Heiniger, J. Müller, Supraleitung und Paramagnetismus in komplexen Phasen der Übergangsmetalle, Helv. Phys. Acta. (34) (1961) 843–858.

[14] A.V. Ruban, H.L. Skriver, J.K. Nørskov, Surface segregation energies in transition-metal alloys, Phys. Rev. B 59 (24) (1999) 15990–16000, https://doi.org/10.1103/PhysRevB.59.15990.

[15] M. Aldén, I.A. Abrikosov, B. Johansson, N.M. Rosengaard, H.L. Skriver, Self-consistent Green's-function technique for bulk and surface impurity calculations: surface core-level shifts by complete screening, Phys. Rev. B 50 (8) (1994) 5131–5146, https://doi.org/10.1103/PhysRevB.50.5131.

[16] A. Chandrasekaran, R.W.E. van de Kruijs, J.M. Sturm, A.A. Zameshin, F. Bijkerk, Nanoscale transition metal thin films: growth characteristics and scaling law for interlayer formation, ACS Appl Mater Interfaces 11 (49) (2019) 46311–46326, https://doi.org/10.1021/acsami.9b14414. Published Online Dec. 2, 2019.

[17] J. Hulva, M. Meier, R. Bliem, Z. Jakub, F. Kraushofer, M. Schmid, U. Diebold, C. Franchini, G.S. Parkinson, Unraveling CO adsorption on model single-atom catalysts, Science 371 (6527) (2021) 375–379, https://doi.org/10.1126/science.abe5757.

[18] Am Molenbroek F. Besenbacher, I. Chorkendorff, B.S. Clausen, B. Hammer, J. K. Norskov, I. Stensgaard, Design of a surface alloy catalyst for steam reforming, Science 279 (5358) (1998) 1913–1915, https://doi.org/10.1126/science.279.5358.1913.

[19] H E.C. Sykes, P. Christopher, Recent advances in single-atom catalysts and single-atom alloys: opportunities for exploring the uncharted phase space in-between, Curr Opin Chem Eng 29 (2020) 67–73, https://doi.org/10.1016/j.coche.2020.06.004.

[20] G.K. Wertheim, S.B. DiCenzo, Cluster growth and core-electron binding energies in supported metal clusters, Phys. Rev. B 37 (2) (1988) 844–847, https://doi.org/10.1103/PhysRevB.37.844.

[21] J.F. van der Veen, F.J. Himpsel, D.E. Eastman, Chemisorption-induced 4f -core-electron binding-energy shifts for surface atoms of W(111), W(100), and Ta(111), Phys. Rev. B 25 (12) (1982) 7388–7397, https://doi.org/10.1103/PhysRevB.25.7388.

[22] D.M. Riffe, G.K. Wertheim, Ta(110) surface and subsurface core-level shifts and 4f7/2 line shapes, Phys. Rev. B 47 (11) (1993) 6672–6679, https://doi.org/10.1103/PhysRevB.47.6672.

[23] 2004 24th International Conference On Microelectronics (IEEE Cat. No.04TH8716), IEEE, 2004.

[24] Z. Awaludin, J.G. Sheng Moo, T. Okajima, T. Ohsaka, TaOx-capped Pt nanoparticles as active and durable electrocatalysts for oxygen reduction, J. Mater. Chem. A 1 (46) (2013) 14754, https://doi.org/10.1039/C3TA12492D.

[25] E. Atanassova, D. Spassov, X-ray photoelectron spectroscopy of thermal thin Ta2O5 films on Si, Appl. Surf. Sci. 135 (1–4) (1998) 71–82, https://doi.org/10.1016/S0169-4332(98)00278-5.

[26] Benito, N.; Palacio, C. Nanostructuring of Ta2O5 surfaces by low energy Ar+ bombardment. *Appl. Surf. Sci.* 2015, 351, 753–759. DOI: 10.1016/j.apsusc.2015.05.143.

[27] Y. Zhang, J.R.G. Evans, S. Yang, Corrected values for boiling points and enthalpies of vaporization of elements in handbooks, J. Chem. Eng. Data 56 (2) (2011) 328–337, https://doi.org/10.1021/je1011086.

[28] S. Abbet, K. Judai, L. Klinger, U. Heiz, Synthesis of monodispersed model catalysts using softlanding cluster deposition, Pure Appl. Chem. 74 (9) (2002) 1527–1535, https://doi.org/10.1351/pac200274091527.

[29] C. Guillot, D. Chauveau, P. Roubin, J. Lecante, M.C. Desjonquères, G. Tréglia, D. Spanjaard, Core level spectroscopy of the low index faces of Tantalum, Surf. Sci. 162 (1–3) (1985) 46–50, https://doi.org/10.1016/0039-6028(85)90874-X.

[30] F. Loi, M. Pozzo, L. Sbuelz, L. Bignardi, P. Lacovig, E. Tosi, S. Lizzit, A. Kartouzian, U. Heiz, D. Alfè, A. Baraldi, Oxidation at the sub-nanoscale: oxygen adsorption on graphene-supported size-selected Ag clusters, J. Mater. Chem. A 10 (27) (2022) 14594–14603, https://doi.org/10.1039/D2TA02539F.

[31] C. Puglia, A. Nilsson, B. Hernnäs, O. Karis, P. Bennich, N. Mårtensson, Physisorbed, chemisorbed and dissociated O2 on Pt(111) studied by different core level spectroscopy methods, Surf. Sci. 342 (1–3) (1995) 119–133, https://doi.org/10.1016/0039-6028(95)00798-9.

[32] R. Simpson, R.G. White, J.F. Watts, M.A. Baker, XPS investigation of monatomic and cluster argon ion sputtering of tantalum pentoxide, Appl. Surf. Sci. 405 (2017) 79–87, https://doi.org/10.1016/j.apsusc.2017.02.006.

[33] C.J. Powell, Practical guide for inelastic mean free paths, effective attenuation lengths, mean escape depths, and information depths in x-ray photoelectron spectroscopy, J. Vacuum Sci. Technol. A 38 (2) (2020), https://doi.org/10.1116/1.5141079.

[34] N.V. Smith, H.H. Farrell, M.M. Traum, D.P. Woodruff, D. Norman, M.S. Woolfson, B.W. Holland, Photoelectron diffraction effects in core-level photoemission from Na and Te atoms adsorbed on Ni(001), Phys. Rev. B 21 (8) (1980) 3119–3130, https://doi.org/10.1103/PhysRevB.21.3119.

[35] S. Lizzit, G. Zampieri, L. Petaccia, R. Larciprete, P. Lacovig, E.D.L. Rienks, G. Bihlmayer, A. Baraldi, P. Hofmann, Band dispersion in the deep 1s core level of graphene, Nature Phys 6 (5) (2010) 345–349, https://doi.org/10.1038/nphys1615.

[36] W.F. Egelhoff, I. Jacob, Reflection high-energy electron diffraction (RHEED) oscillations at 77 K, Phys. Rev. Lett. 62 (8) (1989) 921–924, https://doi.org/10.1103/PhysRevLett.62.921.

[37] U. Heiz, F. Vanolli, L. Trento, W.-D. Schneider, Chemical reactivity of size-selected supported clusters: an experimental setup, Review of Scientific Instruments 68 (5) (1997) 1986–1994, https://doi.org/10.1063/1.1148113.

[38] R. Schaub, H. Jödicke, F. Brunet, R. Monot, J. Buttet, W. Harbich, Decorated Ag19 on Pt(111) or the "rare gas necklace", Phys. Rev. Lett. 86 (16) (2001) 3590–3593, https://doi.org/10.1103/PhysRevLett.86.3590.

[39] Y. Fukamori, M. König, B. Yoon, B. Wang, F. Esch, U. Heiz, U. Landman, Fundamental Insight into the Substrate-dependent ripening of monodisperse clusters, ChemCatChem 5 (11) (2013) 3330–3341, https://doi.org/10.1002/cctc.201300250.

[40] G.K. Wertheim, Core-electron binding energies in free and supported metal clusters, Z. Physik B - Condensed Matter 66 (1) (1987) 53–63, https://doi.org/10.1007/BF01312762.

[41] K. Krupski, M. Moors, P. Jóźwik, T. Kobiela, A. Krupski, Structure determination of Au on Pt(111) surface: LEED, STM and DFT study, Materials 8 (6) (2015) 2935–2952, https://doi.org/10.3390/ma8062935.

[42] A. Baraldi, Structure and chemical reactivity of transition metal surfaces as probed by synchrotron radiation core level photoelectron spectroscopy, J. Phys.: Condens. Matter 20 (9) (2008) 93001, https://doi.org/10.1088/0953-8984/20/9/093001.

[43] A. Baraldi, L. Bianchettin, E. Vesselli, S.d. Gironcoli, S. Lizzit, L. Petaccia, G. Zampieri, G. Comelli, R. Rosei, Highly under-coordinated atoms at Rh surfaces: interplay of strain and coordination effects on core level shift, Phys. Rev. Lett. 9 (5) (2007) 143, https://doi.org/10.1088/1367-2630/9/5/143.

[44] de A. Baraldi, L. Bianchettin, S. Gironcoli, E. Vesselli, S. Lizzit, L. Petaccia, G. Comelli, R. Rosei, Enhanced chemical reactivity of under-coordinated atoms at Pt−Rh bimetallic surfaces: a spectroscopic characterization, J. Phys. Chem. C 115 (8) (2011) 3378–3384, https://doi.org/10.1021/jp110329w.

[45] R. Kodiyath, G.V. Ramesh, E. Koudelkova, T. Tanabe, M. Ito, M. Manikandan, S. Ueda, T. Fujita, N. Umezawa, H. Noguchi, K. Ariga, H. Abe, Promoted C–C bond cleavage over intermetallic TaPt 3 catalyst toward low-temperature energy extraction from ethanol, Energy Environ. Sci. 8 (6) (2015) 1685–1689, https://doi.org/10.1039/c4ee03746d.

[46] D.I. Jerdev, B.E. Koel, Fe deposition on Pt: a route to Fe-containing Pt–Fe alloy surfaces, Surf Sci 513 (1) (2002) L391–L396, https://doi.org/10.1016/S0039-6028(02)01105-6.

[47] *Solid Surface Physics* J. Hölzl, F.K. Schulte, Work function of metals, in: J. Hölzl, F. K. Schulte, H. Wagner (Eds.), Springer Tracts in Modern Physics, Springer Berlin Heidelberg, 1979, pp. 1–150, https://doi.org/10.1007/BFb0048919.

[48] F. Cyrot-Lackmann, On the electronic structure of liquid transitional metals, Adv Phys 16 (63) (1967) 393–400, https://doi.org/10.1080/00018736700101495.

[49] O. Kerrec, D. Devilliers, H. Groult, P. Marcus, Study of dry and electrogenerated Ta2O5 and Ta/Ta2O5/Pt structures by XPS, Materials Science and Engineering: B 55 (1–2) (1998) 134–142, https://doi.org/10.1016/S0921-5107(98)00177-9.

[50] W. Ranke, Low temperature adsorption and condensation of O2, H2O and NO on Pt (111), studied by core level and valence band photoemission, Surf Sci 209 (1–2) (1989) 57–76, https://doi.org/10.1016/0039-6028(89)90058-7.

[51] M. Kiskinova, G. Pirug, H.P. Bonzel, Adsorption and decomposition of H2O on a K-covered Pt(111) surface, Surf Sci 150 (2) (1985) 319–338, https://doi.org/10.1016/0039-6028(85)90649-1.

[52] V.R.R. Medicherla, S. Majumder, D. Paramanik, S. Varma, Formation of self-organized Ta nano-structures by argon ion sputtering of Ta foil: XPS and AFM study, J Electron Spectros Relat Phenomena 180 (1–3) (2010) 1–5, https://doi.org/10.1016/j.elspec.2010.02.006.

[53] Y. Abbas, Y.-R. Jeon, A.S. Sokolov, S. Kim, B. Ku, C. Choi, Compliance-free, digital set and analog reset synaptic characteristics of sub-tantalum oxide based neuromorphic device, Sci Rep 8 (1) (2018) 1228, https://doi.org/10.1038/s41598-018-19575-9. Published Online: Jan. 19, 2018.

[54] I. Perez, V. Sosa, F.G. Perera, J.T. Elizalde Galindo, J.L. Enríquez-Carrejo, P. G. Mani González, Effect of ion bombardment on the chemical properties of crystalline tantalum pentoxide films, Vacuum 165 (2019) 274–282, https://doi.org/10.1016/j.vacuum.2019.04.037.

[55] K. Reichelt, X. Jiang, The preparation of thin films by physical vapour deposition methods, Thin Solid Films 191 (1) (1990) 91–126, https://doi.org/10.1016/0040-6090(90)90277-K.

[56] Physical vapor deposition, The Materials Science of Semiconductors; Rockett, A., Ed, Springer US, 2008, pp. 505–572, https://doi.org/10.1007/978-0-387-68650-9_11.

[57] A. Goldoni, A. Baraldi, G. Comelli, F. Esch, R. Larciprete, S. Lizzit, G. Paolucci, Morphology and magnetic properties of thin films of Rh on highly oriented pyrolitic graphite, Phys. Rev. B 63 (3) (2000) 511, https://doi.org/10.1103/PhysRevB.63.035405.

[58] de L. Bianchettin, A. Baraldi, S. Gironcoli, E. Vesselli, S. Lizzit, L. Petaccia, G. Comelli, R. Rosei, Core level shifts of undercoordinated Pt atoms, J Chem Phys 128 (11) (2008) 114706, https://doi.org/10.1063/1.2841468.

[59] S. Doniach, M. Sunjic, Many-electron singularity in X-ray photoemission and X-ray line spectra from metals, J. Phys. C 3 (2) (1970) 285–291, https://doi.org/10.1088/0022-3719/3/2/010.

[60] G.H. Major, N. Fairley, P.M.A. Sherwood, M.R. Linford, J. Terry, V. Fernandez, K. Artyushkova, Practical guide for curve fitting in x-ray photoelectron spectroscopy, J. Vacuum Sci. Technol. A (6) (2020) 38, https://doi.org/10.1116/6.0000377.

[61] M. Bianchi, D. Cassese, A. Cavallin, R. Comin, F. Orlando, L. Postregna, E. Golfetto, S. Lizzit, A. Baraldi, Surface core level shifts of clean and oxygen covered Ir(111), New J. Phys. 11 (6) (2009) 63002, https://doi.org/10.1088/1367-2630/11/6/063002.

[62] E. Miniussi, E.R. Hernández, M. Pozzo, A. Baraldi, E. Vesselli, G. Comelli, S. Lizzit, D. Alfé, Non-local effects on oxygen-induced surface core level shifts of *Re*(0001), J. Phys. Chem. C 116 (44) (2012) 23297–23307, https://doi.org/10.1021/jp304838g.
[63] G. Kresse, J. Hafner, Ab initio molecular dynamics for liquid metals, Phys. Rev. B 47 (1) (1993) 558–561, https://doi.org/10.1103/PhysRevB.47.558.
[64] G. Kresse, J. Furthmüller, Efficient iterative schemes for ab initio total-energy calculations using a plane-wave basis set, Phys. Rev. B 54 (16) (1996) 11169–11186, https://doi.org/10.1103/physrevb.54.11169.
[65] G. Kresse, D. Joubert, From ultrasoft pseudopotentials to the projector augmented-wave method, Phys. Rev. B 59 (3) (1999) 1758–1775, https://doi.org/10.1103/PhysRevB.59.1758.
[66] P.E. Blöchl, Projector augmented-wave method, Phys. Rev. B 50 (24) (1994) 17953–17979, https://doi.org/10.1103/PhysRevB.50.17953.
[67] J.P. Perdew, K. Burke, M. Ernzerhof, Generalized gradient approximation made simple, Phys. Rev. Lett. 77 (18) (1996) 3865–3868, https://doi.org/10.1103/PhysRevLett.77.3865.
[68] M.V. Ganduglia-Pirovano, J. Kudrnovský, M. Scheffler, Adlayer core-level shifts of random metal overlayers on transition-metal substrates, Phys. Rev. Lett. 78 (9) (1997) 1807–1810, https://doi.org/10.1103/PhysRevLett.78.1807.
[69] J.R. Smith, F.J. Arlinghaus, J.G. Gay, Core-electron binding-energy shifts at surfaces, Phys. Rev. B 26 (2) (1982) 1071–1074, https://doi.org/10.1103/PhysRevB.26.1071.
[70] M. Aldén, H.L. Skriver, I.A. Abrikosov, B. Johansson, Origin of metallic surface core-level shifts, Phys. Rev. B 51 (3) (1995) 1981–1984, https://doi.org/10.1103/PhysRevB.51.1981.
[71] M. Weinert, R.E. Watson, Core-level shifts in bulk alloys and surface adlayers, Phys. Rev. B 51 (23) (1995) 17168–17180, https://doi.org/10.1103/PhysRevB.51.17168.